

Symmetric magnetization reversal in polycrystalline exchange coupled systems via simultaneous processes of coherent rotation and domain nucleation

Amitesh Paul,^{1,*} C. Schmidt,² N. Paul,³ A. Ehresmann,² Stefan Mattauch,⁴ and Peter Böni¹

¹*Technische Universität München, Physik Department E21, Lehrstuhl für Neutronenstreuung, James-Frank-Straße 1, D-85748 Garching b. München, Germany*

²*Universität Kassel, Institut für Physik and Centre for Interdisciplinary Nanostructure Science and Technology (CINSaT), Experimentalphysik IV, Heinrich-Plett-Strasse 40, D-34132 Kassel, Germany*

³*Helmholtz-Zentrum Berlin für Materialien und Energie GmbH, Hahn-Meitner-Platz 1, D-14109 Berlin, Germany*

⁴*Jülich Centre for Neutron Science Forschungszentrum Jülich GmbH, Außenstelle am FRM-II c/o TU München, Lichtenbergstraße 1, D-85747 Garching b. München, Germany*

(Received 9 May 2012; published 14 September 2012)

Training in exchange bias systems plays an essential role in understanding the very origin of the biasing effect. The nonequilibrium arrangement of antiferromagnetic (AF) spins at the antiferromagnetic-ferromagnetic interface, related to the AF uniaxial anisotropy, plays a crucial role during the initial training. Our system of choice, IrMn/CoFe, possesses softer uniaxial anisotropy compared to other AF systems (e.g., CoO), thereby reducing the energy penalty due to nonequilibrium spins. Different methods have been applied to initialize or modify the unidirectional anisotropy. We apply an in-plane field (a) during field growth, (b) during field cooling below its blocking temperature, and (c) in an in-plane magnetic field during ion irradiation, along and opposite the field applied during field growth. Magnetization reversal mechanisms were investigated during the first two field cycles to identify the role of each method on the training. A detailed analysis of polarized neutron scattering using the distorted wave Born approximation reveals a simultaneous process of domain nucleation and coherent rotation for magnetization reversal.

DOI: [10.1103/PhysRevB.86.094420](https://doi.org/10.1103/PhysRevB.86.094420)

PACS number(s): 75.70.Cn, 75.30.Gw, 61.80.Jh

I. INTRODUCTION

The basic understanding of the origin of the exchange bias (EB) effect has been summarized in recent reviews.^{1,2} Interfacial exchange coupling between a ferromagnet and an antiferromagnet can “lock” the magnetic moments of the ferromagnet in a well-defined direction, which makes the system biased.³ Exchange bias is associated with many salient features, such as coercivity enhancement,^{4,5} asymmetric hysteresis loops,^{6–8} and training effects.^{9,10} Conventionally, a cooling field H_{FC} applied during cooling below the ordering temperature T_N of the antiferromagnet determines the direction and strength of the unidirectional anisotropy characterized by the exchange bias field H_{EB} .^{7,11} The measured bias is proportional to the projection of the frozen-in antiferromagnetic (AF) spins onto the cooling field (H_{FC}) direction, which in most cases is also the ferromagnetic (FM) easy axis.

A. Training effects and anisotropies

Generally, two types of training effects can be distinguished: a relatively large training can be seen between the first and second loop, and a comparatively small effect can be seen for the subsequent higher number of loops. The first type has been demonstrated experimentally to arise from the AF magnetic symmetry.¹⁰ For the second type, it has been shown that $H_{EB} \sim (n)^{-1/2}$ (for $n > 2$), where n is the number of loops.

The strong training behavior between the first and second hysteresis loop is usually attributed to some initial nonequilibrium arrangement or metastable state of the AF spins. The exact mechanism for the initial AF spin arrangement is still a matter of debate. Hoffmann¹² employed a coherent

rotation model to identify biaxial anisotropy axes in the AF as a recompensable factor for the noncollinear arrangement of the AF (sublattice) spins. These spins, initially stabilized after field cooling (FC), lead to a sharp drop in the coercive field along the descending field branch of the first hysteresis loop as the AF spins relax into a collinear arrangement. Note that this first loop training effect is also associated with the so called asymmetric magnetization reversal along the decreasing and increasing branches of the hysteresis loops. This means that a system without any inherent frustration may not be liable to exhibit such asymmetry in magnetization reversal. Micromagnetic calculations by Saha *et al.*, on the other hand, did not rule out training but showed symmetric magnetization reversal for uniaxial systems which are without biaxial anisotropy from any inherent frustration.¹³ Their calculations, however, do agree with Hoffmann’s calculations in the case of biaxially anisotropic systems. Beckmann *et al.*¹⁴ have shown that a misalignment between the cooling field direction and the easy axis of the antiferromagnet can result in a nonequilibrium arrangement of the AF spins with a net magnetization oriented in a direction other than the AF easy axis. This is basically determined by the relative orientations between the cooling field and the AF easy axis. This effect also leads to asymmetry in magnetization reversal. Thus training—particularly that between the first and the second field cycles—can be primarily related to magnetocrystalline anisotropy in the antiferromagnet and its frustration.

It is suggested that the reconfiguration of the AF moments or domains during the field cycling is the reason for the second type of training. Very recently, detailed data analysis of diluted CoO has shown that the training effect of the CoO/Co bilayer has its origin in the training of the irreversible surplus

thermoremanent magnetization.¹⁵ This is, in fact, in agreement with Binek's model¹⁶ in the thermodynamic framework of a relaxed spin configuration within the antiferromagnet. However, the agreement was restricted again to $n > 1$.

B. Training effect and cooling field

Paul *et al.*¹¹ have shown that the training effect in exchange bias systems can be strongly influenced by the cooling field. It basically stems from the domain state that the FM layer attains depending upon the strength of the field during cooling. For example, in the absence of a field, a multidomain state is formed which may suppress the training, whereas with a saturating field, a single domain state is formed and thereby the training effect is prominent. The idea is that in the absence of any field, random orientations of exchange coupled AF grains may have local anisotropic directions that are different from those of the FM magnetization direction.^{17,18} On the other hand, application of a sufficiently strong external field can lead to a macroscopic net magnetization—originating from the exchange interaction between uncompensated spins.¹⁹ In such a case, the local anisotropy axis is obviously oriented along the cooling field direction. Following this, it was also conjectured that an antiferromagnet with strong uniaxial anisotropy (such as CoO) may be more susceptible to training than an antiferromagnet with no or insignificant uniaxial anisotropy.^{9,20}

C. Training effect and field-induced growth

It is also known that a magnetic field during growth can alternatively induce magnetocrystalline anisotropy in the system (directional ordering) that would otherwise be isotropic. Thus the field applied to define the induced unidirectional anisotropy in an exchange coupled system can also influence the uniaxial anisotropy, which in turn may affect its training behavior. Such growth-induced magnetocrystalline anisotropy is common in magnetron sputtered samples as the magnetic field applied during sputtering and also the magnetic field configuration used to confine the plasma²¹ may even contribute to its directional preference.

D. Training effect and ion irradiation

A very similar situation may arise when the system is subjected to low or moderate energy ion irradiation. For many scientific communities, “low energy” is of the order of a few eV to a few hundreds of eV as opposed to a few tens of keV for moderate energy ions or MeV and above for high energies. During ion irradiation, part of the energy from the electronic system is transferred to the lattice via electron-phonon coupling. This results in a rise in the local temperature along the ion track (which is referred to as a thermal spike and is suitable for metals) crossing the melting temperature of the material. Thus application of a field during ion irradiation will also redefine the unidirectional anisotropy.

E. Training and anisotropies in IrMn

Exchange bias systems containing an antiferromagnet with Néel temperatures T_N far above room temperature are of high importance for practical applications. Mn-based binary alloys such as FeMn, IrMn, PdMn, PtMn, and NiMn are particularly

relevant because of their excellent corrosion resistance and large bias fields.²² Apart from the classical Co/CoO-based system, which has been a regular system of choice,^{23–25} IrMn-based systems are interesting due to their room-temperature ordering, which enables the behavior of antiferromagnetically ordered moments to be investigated at room temperature.²⁶

It may be interesting to note that in the IrMn/CoFe system, asymmetric magnetization reversal has often been reported²⁷ along with symmetric reversal.⁸ Complex small-scale domains usually dominate the reversal processes for IrMn samples along with variation in the orientation of domain walls along the two branches of the hysteresis loop.^{18,28,29} Interestingly, two energy barrier distributions with different time constants were predicted to coexist. Thermally activated reversal of the AF layer with a large time constant results in an increasing shift of the entire hysteresis loop.^{30,31} Thermal activation with a small time constant was believed to contribute to loop broadening, an asymmetry in reversal, and training effects.³² This may be indicative of the fact that uniaxial anisotropy is often associated intrinsically with the system, i.e., it is responsible for the asymmetry in reversal and the subsequent training. This may be the reason behind the lack of macroscopic training in IrMn- or FeMn-based exchange bias systems. One may note that IrMn and FeMn are not ordered AF materials, unlike, e.g., NiMn or PtMn. In polycrystalline samples, in a state where the thermal fluctuations can be neglected, the reversal of the FM layer can be inhomogeneous due to interactions with the AF grains with random anisotropy directions.

Thus to investigate the effect of the induced unidirectional anisotropy without the effect of uniaxial anisotropy on training, one needs to investigate the magnetization reversal mechanism in a system with at least a comparatively much smaller uniaxial anisotropy, such as IrMn. With a Cu underlayer, it can go up to $\sim 5.25 \times 10^6$ erg/cm³.³³ Note, for comparison, that the uniaxial anisotropy of CoO is $\sim 25 \times 10^7$ erg/cm³.³⁴

The FM uniaxial anisotropy is two orders of magnitude lower ($\sim 2 \times 10^4$ erg/cm³). In this way, any training in the system can be considered to be virtually independent of its *intrinsic* uniaxial anisotropy and can be attributed only to the effect of field cooling or growth or ion irradiation inducing the unidirectional anisotropy.

The primary aim of this study is, therefore, to investigate the magnetization reversal mechanism in the untrained as well as the trained specimens to identify the role of unidirectional anisotropy and field-induced *extrinsic* uniaxial anisotropy by complying the different conditions defining the unidirectional anisotropy on exchange coupling. The strong influence of the *intrinsic* uniaxial AF anisotropy on training (such as that in CoO/Co systems) will be regarded as negligible in our system of choice: IrMn with a Cu underlayer grown without any inherent magnetic field in the deposition system. We have taken various ways to define or redefine the unidirectional anisotropy and its direction. This is done by application of a field:

- (i) During the growth of the sample (H_{FG}).
- (ii) During the growth of the sample and also after heating the sample above its ordering temperature and cooling below (H_{FGFC}).

(iii) During the growth of the sample and during ion irradiation (H_{FGIB0}) parallel to the applied field.

(iv) During the growth of the sample and during ion irradiation in an opposite direction to H_{FG} (H_{FGIB180}).

F. Ion irradiation

The slowing down of ions in solids results from energy loss in solids. This can be caused either by inelastic collisions with electrons [S_e (keV/nm) = electronic stopping power] or by elastic collisions with the nuclei of the target atoms [S_n (keV/nm) = nuclear stopping power]. Ion irradiation, in particular, has proven to be a unique way of redefining the unidirectional anisotropy axis: Ion irradiation in an applied in-plane magnetic field H_{IB} can be used to change the exchange bias field H_{EB} and the coercivity H_C of exchange coupled AF/FM thin films initialized by field cooling or field growth (FG). Depending upon the ion dose and the direction of H_{IB} with respect to the direction of H_{EB} , it is possible to increase or reduce H_{EB} as well as, e.g., to change the direction of H_{EB} .^{17,35,36} The origin of this effect may be explained by three processes using a two-energy-level model, where the two levels are separated by an energy barrier.^{18,35}

(i) Ion irradiation deposits locally orders of magnitude more energy per atom as compared to thermal energy deposition (e.g., by field cooling). Due to this, grains with a high energy barrier surpass this barrier and contribute to the EB effect.

(ii) The energy barrier depends on the local anisotropy constant (K_{AF}) of the AF grain and the effective magnetic volume over which the AF anisotropy extends. Ion irradiation induces defects in the antiferromagnet or destroys the order of the antiferromagnet. Therefore, the energy barrier is reduced, enabling grains with formerly high barriers to surpass the now reduced energy barrier with thermal excitations.

(iii) Ion irradiation induces defects at the interface and/or causes interface intermixing between the AF grains and the FM layer, which destroys the interface coupling and causes H_{EB} to decrease.³⁷ This can lead to a complete suppression of the EB effect.

These three effects occur simultaneously at ion irradiation of exchange coupled thin layers, but one effect always dominates depending on the ion dose.

One may note that we are using light ions, i.e., ions with low nuclear charge. Please also note that the present technique not only employs ion irradiation, but an irradiation in an applied magnetic field, and it is not the implantation (i.e., a compositional change of the layer system by the additional implanted ions) but the energy transfer which changes the system either by excitation of the electronic system or by defect creation/intermixing. Ion irradiation affects in principle the exchange bias system. The observed modifications can be explained in terms of defect creation acting as pinning sites for domain walls and atomic intermixing. All these structural properties are modified due to the energy loss of the ions in the solid along their trajectory. The mechanisms involved in these processes rely on changes in the structural properties, the interface abruptness, the chemical composition of the films, and the degree of chemical ordering in alloys. In the “low or

moderate energy range,” the energy loss is usually below the threshold of intermixing.³⁸

A second aim of this study is to show how the moderate energy ion irradiation changes the exchange coupled system. This is particularly interesting as the ion energy used for irradiation is only 10 keV. Conventional ion irradiation (keV) produces an electronic stopping power of a few keV/nm and therefore ion track damage does not occur. The electronic energy loss S_e in the system is below 7 keV/nm, which is far below the threshold of damage production. Metals like Fe and Co have a certain sensitivity to S_e that varies around a few tens of keV/nm.³⁹ Using a depth-sensitive technique, one can easily visualize the effect of ion irradiation on magnetic domains. Such an effect is otherwise heavily shrouded by the strong interfacial structural modification. In the present study, this is made possible as we compare the magnetization reversal of a 10 keV ion-irradiated system with that of a conventional field-cooled one.

II. EXPERIMENTAL DETAILS

The $\text{Ir}_{17}\text{Mn}_{83}$ (10 nm)/ $\text{Co}_{70}\text{Fe}_{30}$ (5 nm)/Ta (8 nm) films were deposited by rf sputtering onto naturally oxidized Si(100) substrates with a buffer layer of 50 nm Cu. The samples for each biasing condition were from the same Si piece (broken after deposition for various measurements). Thus the untrained and the trained samples are from the same set. Each of the biasing sets was deposited separately as they were treated differently. The base pressure was 1.0×10^{-6} mbar and the Ar pressure during deposition was 1.5×10^{-3} mbar (Ar flow of 80.1 sccm). For field growth, an in-plane magnetic field of $H_W = 99.27$ Oe (7.9 kA/m) was applied during the deposition process. The initialization by field cooling was performed in an in-plane magnetic field of $H_{\text{FC}} = 502.65$ Oe (40 kA/m): after heating to 275 °C for 60 min in vacuum (2.5×10^{-6} mbar), the samples were cooled down to room temperature within 20 min. A vibrating sample magnetometer (VSM) was used to characterize the sample’s magnetization reversal. The in-plane magnetic field range during characterization was ± 841.94 Oe (67 kA/m). The applied magnetic field was in the sample plane parallel to the easy axis. The microstructure and the layer quality are investigated by low angle x-ray reflectivity (XRR).^{40–42}

A. Ion irradiation

Irradiations were performed at room temperature. We used a home-built ion source at the University of Kassel for the irradiation with 10 keV He^+ ions (only singly ionized).⁴³ Briefly, He gas is fed via a flow controller into a Penning source, where it is ionized in a high-voltage electrical field. A constant magnetic field of 500 Oe was used during the irradiation process.

B. Neutron scattering measurements

Depth-sensitive polarized neutron reflectivity (PNR) measurements have been performed at the polarized neutron reflectometer with polarization analysis TREFF at the Jülich Center for neutron Research FRM-2. The neutron wavelength has been fixed at $\lambda = 4.73$ Å. The instrument details are

described elsewhere.⁴⁴ The specimens are kept at room temperature and an external field H_a of up to 1.5 kOe has been applied. The direction of H_a is in the plane of the bilayer and perpendicular to the in-plane uniaxial easy axis of the magnetization determined from magnetization measurements. We perform PNR measurements at four different strengths H_a of the applied field along one branch of the hysteresis loop.

Due to the interaction between polarized neutrons and magnetic moments in the specimen, PNR is sensitive to the in-plane magnetization for a homogeneous film on a *microscopic* scale. Neutron scattering with polarization analysis can discriminate between the longitudinal and transverse components of magnetization. The neutron interaction potential is given by

$$V = \frac{2\pi\hbar^2}{m}(\rho_n \pm \rho_m) = \frac{2\pi\hbar^2}{m}Nb_n + \mu_N\vec{\sigma} \cdot \vec{B}, \quad (1)$$

where N ($=\rho_0 N_A |M|^{-1} \text{ cm}^{-3}$) is the number density, b_n is the coherent nuclear scattering length, m is the neutron mass, $|M|$ is the atomic mass (gm mol^{-1}), ρ_0 is the mass density (gm/cm^3), N_A is the Avogadro number ($6.023 \times 10^{23} / \text{mol}^{-1}$), B is the internal magnetic field of the specimen, and $\vec{\sigma}$ represents the operator associated with the Pauli spin matrices while μ_N represents the nuclear magneton. The neutron magnetic moment is expressed as $\mu_n = -g_n \mu_N S_n$, where S_n ($=\vec{\sigma}/2$) is the spin- $\frac{1}{2}$ operator and g_n is the g factor of the nucleon related to the gyromagnetic ratio γ_N ($=1.913$). The scattering-length densities (SLD) of a magnetic specimen are given by either the sum or difference of the nuclear (ρ_n) and magnetic (ρ_m) components. The \pm signs refers to the spin-up and spin-down states of the incident neutron with respect to the spin polarization of the specimen.

A detailed description of the technique and measurements can be found in Ref. 45. In specular scattering geometry, the normal wave vector transfers $q_{\perp} = \frac{2\pi}{\lambda} [\sin(\alpha_i) + \sin(\alpha_f)]$ are probed while off-specular scattering contributions along the in-plane momentum transfer vector $q_{\parallel} = \frac{2\pi}{\lambda} [\cos(\alpha_f) - \cos(\alpha_i)]$ arise when the in-plane translational symmetry is broken by interface waviness (roughness) or by magnetic domains on a length scale shorter than the neutron coherence length (l_{\parallel}) along q_{\parallel} . The non-spin-flip (NSF) scattering amplitude provides information about $\rho_n \pm \rho_m \cos\phi_A$, and the spin-flip (SF) channels measure $\rho_m^2 \sin^2\phi_A$ if the domain size is larger than the projection of the neutron coherence length along the sample plane (l_{\parallel}). Here, ϕ_A is the angle between the magnetization M and the applied field H_a (which is the neutron quantization axis). In the experiment, four different cross sections can be distinguished: NSF (R_{++} and R_{--}) and SF (R_{+-} and R_{-+}) channels. Here + and - signs are used to distinguish the intensity contributions R representing a polarization component \parallel or anti- \parallel to the guiding field, respectively. $R_{++/-}$ contains the sum/difference between the nuclear (ρ_n) and magnetic scattering (ρ_m), whereas the SF signal contains only the magnetic information. Even though the measurement time is around 24 h, the thermal activation processes within the antiferromagnet can be neglected in the present case. A thicker AF layer leads to increased stability of the AF domains.

We employ the distorted wave Born approximation (DWBA) to simulate the off-specular scattering.⁴⁵ In our model, the mean magnetization with respect to the applied field varies from region to region around a mean angle ϕ_A with a Gaussian distribution of width $\Delta\phi_A$. In this model, both the components of magnetization parallel (along the y axis) and perpendicular (along the x axis) to H_a will contribute to the diffuse scattering signal.

III. RESULTS AND DISCUSSION

A. Ion irradiation

Calculations using the TRIM (transport of ions in matter) code⁴⁶ indicate that 10 keV He ions are implanted in the Cu underlayer, as the implantation depth is ~ 35 nm. Figure 1(a) shows the impact on the ion trajectory for 10 keV ions within the layered system. For the 10 keV He⁺ ions, the trajectory is rather widely distributed. One can see that the interfaces are the locations of maximum attenuation for the ions as they traverse through the multilayer. Figure 1(b) shows almost the same order of electronic and nuclear energy losses (for 10 keV He ions as calculated by TRIM). The $1 \times 1 \text{ cm}^2$ samples were irradiated uniformly by a fluence of 10^{14} ions/cm² by scanning the ion beam using an electromagnetic scanner at 10^{-6} torr of pressure in the chamber.

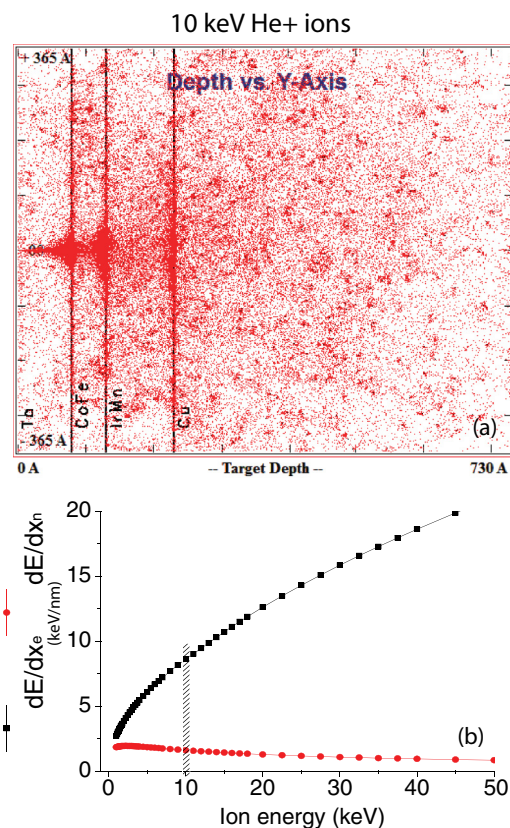


FIG. 1. (Color online) (a) TRIM simulations for 1×10^3 He ions on our target showing the trajectory in the case of 10 keV energy. (b) Electronic energy loss as compared to that of nuclear energy loss for 10 keV He ion irradiation. The dotted line indicates the energy used and thereby the expected range of electronic and nuclear energy losses within the target.

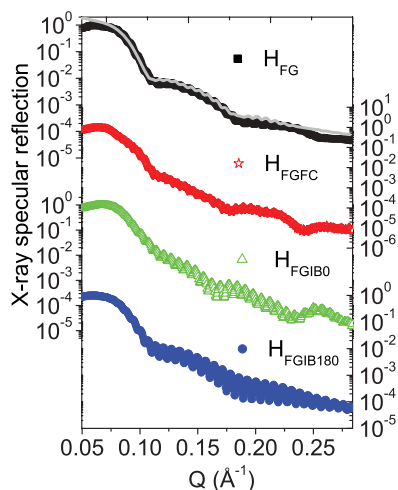


FIG. 2. (Color online) Specular XRR scans of the samples for different biasing conditions. The curves are vertically shifted for clarity. The fit to the first pattern is also shown as a gray line. A magnetic field $H_W = 99.27$ Oe (7.9 kA/m) was applied during the growth of each sample.

B. XRR

Figure 2 shows the x-ray specular reflectivity (XRR) from the samples. The fits to the sample with H_{FG} are shown. The specular patterns are fitted by the least-squares method using the standard optical formalism according to Nevot and Croce,⁴⁷ as was also described earlier.⁴⁸ Note that we have not considered an interdiffused layer. The quality of the fit justifies such a consideration. The thickness of the individual layers and the average σ ($=1.2$ nm) are determined from the fit. The total thickness oscillations for the $H_{FGIB180}$ sample appear to be more well defined than the rest. This is probably due to the ~ 1.0 nm greater thickness and the slightly improved interface quality. Intermixing at the interface may depend on the deposition conditions used, and thus on factors such as stress in the films which can be affected by low and moderate energy ions even though the electronic energy loss in the system remains low. However, the XRR data for all of our samples indeed support the fact that there is no intermixing induced by the He ions used. This is also the case for the neutron reflectivity data (shown later), where no intermixing between the layers is considered in the fitting model.

C. VSM

Figure 3 shows the VSM hysteresis loops along two perpendicular directions for an as-grown sample (without any unidirectional anisotropy induced): one is along the axis of the magnetic field that is usually applied while growing our samples (easy axis) and another is along the perpendicular direction to the field axis (hard axis). Interestingly, one can see that the two curves are very similar to each other. This clearly indicates that the system, without any external magnetic field, remains in a state with no macroscopic biasing.¹⁷ This, however, does not exclude randomly oriented multiple AF anisotropy axes from AF grains. Interestingly, we do not observe any changes in the coercive fields during several field cycles after the second field cycle.

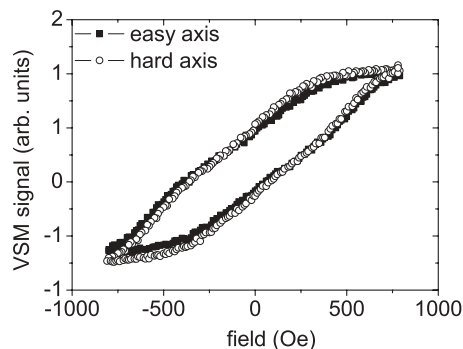


FIG. 3. VSM hysteresis loops along two perpendicular axes showing no uniaxial anisotropy for an as-grown sample.

Figure 4 shows the VSM hysteresis loops for the samples with four different conditions of unidirectional anisotropy induced. The measured bias is known to be proportional to the projection of the frozen-in AF spins onto the H_{FC} direction, which in most cases is also the FM easy axis.

Phenomenologically, for in-plane field cooling, the free energy per unit area of the AF-FM bilayer can be written as

$$E = K_{FM}t_{FM}\sin^2(\delta - \gamma) + K_{AF}t_{AF}\sin^2(\beta - \eta) - J_E M_{AF}M_{FM}\cos\delta - H_a M_{FM}\cos(\delta - \theta)t_{FM}, \quad (2)$$

where the first two terms represent the *uniaxial* anisotropy energies of the FM and AF layers with the anisotropy constants K_{FM} and K_{AF} . The AF anisotropy term, though greater than the J_E term, is assumed to be rigid along its easy axis and is not considered in energy minimization. Also neglected is the

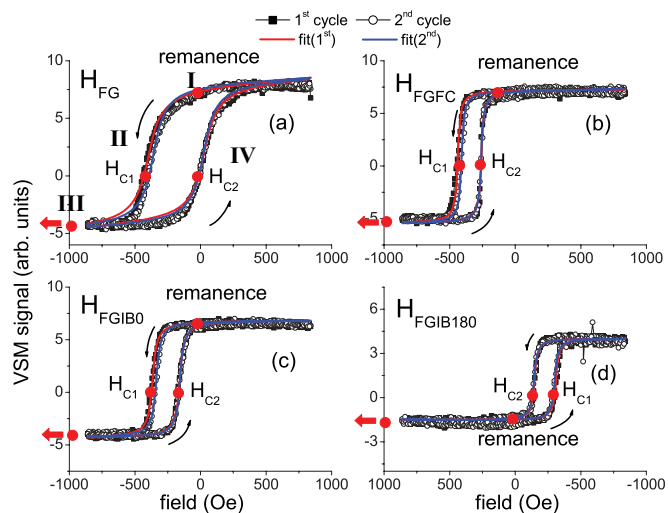


FIG. 4. (Color online) VSM hysteresis loops for four different conditions of unidirectional biasing. The field cycling (marked by arrows) starts and ends at $H_a = +1000$ Oe going through the negative saturation field ($H_a = -1000$ Oe). The red dots (I–IV) indicate the points of neutron scattering measurements for each sample (the measurements for saturation were done at $H_a = -4000$ Oe). The forward and backward branches of the hysteresis loops have been fitted individually by an arctan function shifted for the exchange bias field, from which coercive fields have been determined (red and blue solid lines).

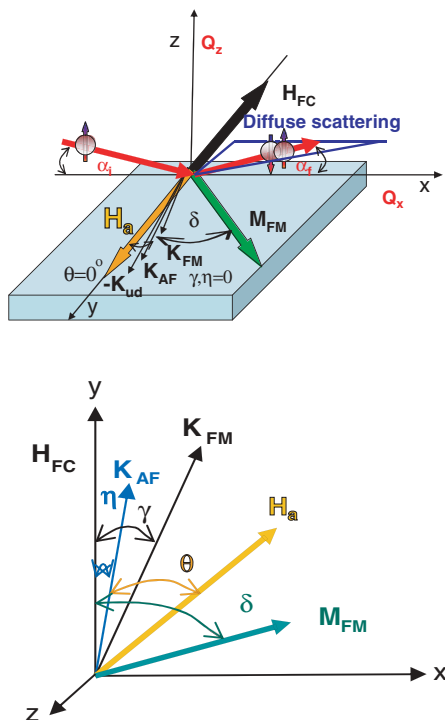


FIG. 5. (Color online) Illustration of the different in-plane anisotropy axes and the scattering geometry. The angles δ and γ in the figure are exaggerated for clarity. An in-plane (x - y) view of the different axes and the angles with respect to the cooling field axis is also shown. In this figure, H_a is shown to be antiparallel to H_{FC} . Here K_{ud} , K_{AF} , and K_{FM} indicate the unidirectional anisotropy, the AF anisotropy, and the FM anisotropy directions, respectively. M_{FM} is the FM magnetization as we neglect the AF magnetization M_{AF} , and thereby the angle β is not shown.

Zeeman term associated with the AF magnetization M_{AF} . The third term is the *unidirectional* anisotropy energy characterized by the exchange coupling constant J_E . The unidirectional anisotropy K_{ud} is embedded in $J_E M_{AF} M_{FM}$ as the exchange field $H_{EB} = J_E M_{AF}$ and interfacial exchange energy $J_{int} = K_{ud} t_{FM}$. Finally, the last term stands for the Zeeman energy for a field H_a . Here δ is the angle between M_{FM} and the easy axis along the y axis, γ is the angle between K_{FM} and H_{EB} , whereas θ is the angle between H_a and the H_{FC} direction, where M_{FM} and M_{AF} are the respective magnetizations. The angle between the H_{FC} direction and the AF anisotropy axis is η and that between the AF magnetization is β . In the case of conventional in-plane field cooling, γ and η are zero (the field cooling axis coincides with the anisotropy axes); θ is generally $\sim 0/180^\circ$

as H_a is applied along the H_{FC} direction. The energy maxima in saturation can be obtained for $\delta = 0^\circ$ and 180° . In these two situations, $H_{C1} = -[(2K_{FM} + J_{int})/M_{FM}t_{FM}]$ and $H_{C2} = [(2K_{FM} - J_{int})/M_{FM}t_{FM}]$. Therefore, $H_{EB} = (H_{C1} + H_{C2})/2$. Thus for $\delta \approx 0^\circ$, one can observe nonuniform magnetization reversal as the angle between the effective field (resultant of the three anisotropy fields along their respective directions) and the M_{FM} direction is small.⁸ It is noteworthy that if the magnetic anisotropy in the AF is low ($K_{AF}t_{AF} < J_{int}$), it is energetically more favorable that during the reversal, the FM and AF spins rotate together and there will be no loop shift. A schematic of the different anisotropy axes corresponding to the in-plane cooling field is shown in Fig. 5.

The fits to the VSM data give the corresponding values of the coercive fields (H_{C1} and H_{C2}) which are along the decreasing branch (H_a opposite to the biasing field direction) and the increasing branch (H_a along the biasing field direction). As the biasing field for $H_{FGIB180}$ is opposite to that of other samples, so are the corresponding decreasing and increasing branches. The coercivity change (H_C , half-width of the hysteresis loop) and the exchange bias field (H_{EB} , shift of the hysteresis loop) are tabulated in Table I.

A quick comparison of the specimens in the *trained* state to that in the *untrained* state apparently indicates that the magnetization profile is very similar along the decreasing as well as the increasing branches. No visible changes for the case $H_{FGIB180}$ are noticed. A small difference in the coercive fields (≈ 10 Oe) between the states for the first field cycle and the second field cycle along the decreasing branch may be noticed, but only after looking carefully, for H_{FG} , H_{FGFC} , and H_{FGIB0} . A similar difference in their exchange bias fields can also be noticed. However, no asymmetry in magnetization reversal, which is a common feature in exchange bias systems with a strong uniaxial anisotropic AF layer, is visible, at least macroscopically. Apparently, along both branches the magnetization reversal takes place via coherent rotation (uniform) and not via domain wall nucleation and motion (nonuniform). This is evident from the rounded shape of the loop, which is basically due to sequential overcoming of the energy barriers due to randomly oriented multiple AF anisotropy axes from AF grains.

One may also note a significant change in the coercive field (H_{C2}) along the increasing branch of the hysteresis loop for the ion-irradiated (from around -20 Oe to ≈ -200 Oe) as well as for the field-cooled sample (from around -20 Oe to ≈ -260 Oe) as compared to the field-grown sample. The value of H_{C1} , however, remains fairly similar around -400 Oe for the nonirradiated samples.

TABLE I. VSM results showing $H_{EB} = (H_{C1} + H_{C2})/2$ and $H_C = (H_{C1} - H_{C2})/2$.

Biasing condition	VSM			
	H_{C1} (Oe) ± 5 (first/second cycle)	H_{C2} (Oe) ± 5 (first/second cycle)	H_{EB} (Oe) ± 5 (first/second cycle)	H_C (Oe) ± 5 (first/second cycle)
H_{FG}	-420/-400	-20/-20	-220/-210	-200/-190
H_{FGFC}	-435/-420	-260/-260	-347/-340	-87/-80
H_{FGIB0}	-375/-356	-200/-200	-267/-258	-107/-98
$H_{FGIB180}$	-315/-315	-130/-130	-222/-222	-92/-92

TABLE II. PNR results showing the respective layer thicknesses, the angle of magnetization ϕ_A at the respective coercive fields, and the degree of training $\delta\phi_A$ at the first coercive field.

Biasing condition	t_{Ta}	t_{CoFe}	t_{IrMn}	t_{Cu}	at H_{C1}	at H_{C2}	at H_{C1}
	(nm)	(nm)	(nm)	(nm)	ϕ_A (deg) ± 5	ϕ_A (deg) ± 5	$\delta\phi_A$ (deg) ± 5
	± 0.1	± 0.1	± 0.1	± 0.1	(first/second cycle)	(first/second cycle)	(ϕ_A (first cycle) $-\phi_A$ (second cycle))
H_{FG}	9.1	5.8	10.2	54.1	$-110/-80$	$-90/-145$	-30
H_{FGFC}	6.1	7.1	9.2	56.2	$-20/-55$	$-110/-90$	35
H_{FGIB0}	8.5	6.3	10.0	56.0	$-130/-110$	$-137/-145$	-20
H_{FGIB180}	13.5	6.9	9.7	59.6	$-30/-145$	$-70/-70$	115

D. Neutron scattering

The fitted values of the thicknesses of individual layers and the respective ϕ_A values, at different field cycles and along different branches of the hysteresis loops, as obtained from the PNR data, for each of the samples are given in Table II. We also show the degree of training as estimated from respective differences in the magnetization directions and expressed as $\delta\phi_A = [\phi_A$ (first cycle) $-\phi_A$ (second cycle)] in Table II.

The ρ_m values at the respective coercive fields and at saturation along with the estimated FM magnetization M_{FM} at saturation are tabulated in Table III. The M_{FM} values are obtained from the fitted values of ρ_m at saturation ($\rho_m = M_{\text{FM}} \times 2.853 \times 10^{-9} \text{ \AA}^{-2} \text{ cm}^3/\text{emu}$). Note that the ρ_n (e.g., CoFe $\rho_n = 3.8 \times 10^{-6} \text{ \AA}^{-2}$) values and the interface roughnesses are kept similar in each case (the dynamical Q range is quite limited in the case of a neutron as compared to that in an x-ray).

1. Sample: H_{FG}

The specular reflectivity patterns of the field grown specimen (closed symbols) are plotted together with their least-squares fits (open circle) in Fig. 6 for four different applied fields. The data R_{--} dominate over R_{++} for the remanence field ~ -20 Oe and vice versa for the saturation field at $+4$ kOe. It is related to a net magnetization, collinear to H_a . From the fits to the data, one may note that the respective layer thicknesses are similar to their nominal thicknesses, and their magnetic profiles (all determined from that at maximum applied field after parallel field cooling) do not vary with field cycling. For all other fields, the only two parameters that were varied are ϕ_A and ρ_m . The FM magnetization directions (indicated by an arrow in the figures) are very different for all the fields of measurements corresponding to the two field cycles.

The fits for the first field cycle reveal that the orientation of ϕ_A is around -180° at a remanence field, and this

becomes $-110^\circ/-90^\circ$ at the respective field values at $H_{C1/C2}$. Similarly, the magnetization direction turns from $-80^\circ/-145^\circ$ when measured along the second field cycle at the respective fields $H_{C1/C2}$, which eventually becomes 0° at saturation. This shows that the degree of uniform (coherent rotation) angular rotations are not very similar for the two field cycles (first and second cycles). They also differ in magnitude when measured at their H_{C2} corresponding to the two field cycles. This is a definitive indication of a small-scale microscopic training in the system. Note that the fields of measurements for the untrained and that of the trained states are exactly the same within the same experimental setup, thus ruling out any change in the applied field axis with respect to the anisotropy axis.

We show the corresponding intensity maps (off-specular and specular SF scattering signals) in Fig. 7. The intensity along the diagonal $\alpha_i = \alpha_f$ is the specular reflection along Q_\perp . These maps are also simulated within the DWBA.⁴⁵ The simulations are done by taking into account the various optical effects, such as reflection and refraction components (spin-up and spin-down) and convoluting with instrumental resolution. The lateral intensities are due to the perturbation considered. The Fourier transform of the pair correlation functions for transverse as well as longitudinal fluctuations (averaging over the surface of the coherence regime and integrating along the unresolved y axis) within a laterally homogenous length scale of $2\xi_{(x,y)}$ can be expressed as functions of Lorentzian shapes.

The value of ϕ_A is taken from the fitted values of the specular patterns. We consider the magnetization to fluctuate from domain to domain around a mean angle ($\Delta\phi_A = 30^\circ$). We observe typical signatures of vertically uncorrelated domains in off-specular scattering along the Yoneda streaks at their coercive fields.⁴⁹ The disappearance of these intensities at saturation confirms their magnetic origin. The simulations to the intensity maps show that for the first field cycle at H_{C1} , the domain size is as small as $0.5 \mu\text{m}$, which increases to around

TABLE III. PNR results showing the magnetic scattering length densities and the calculated magnetization values.

Biasing condition	at H_{C1}	at H_{C2}	at saturation	M_{FM}
	$\rho_m (\times 10^{-6} \text{ \AA}^{-2}) \pm 0.1$	$\rho_m (\times 10^{-6} \text{ \AA}^{-2}) \pm 0.1$	$\rho_m (\times 10^{-6} \text{ \AA}^{-2}) \pm 0.1$	(emu/cm ³)
	(first/second cycle)	(first/second cycle)		
H_{FG}	0.6/1.2	0.8/1.7	2.5	876
H_{FGFC}	1.5/1.5	1.0/2.0	2.0	701
H_{FGIB0}	1.5/1.3	1.5/1.9	3.8	1332
H_{FGIB180}	1.4/1.7	1.5/1.0	2.3	806

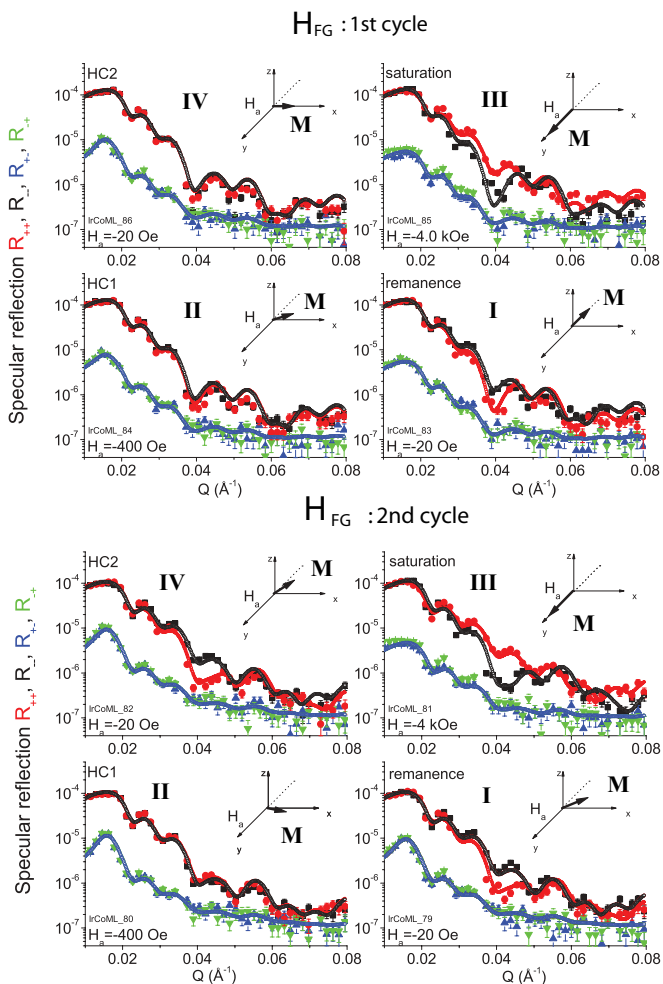


FIG. 6. (Color online) Specular reflectivity patterns (solid symbols) along with their fits (open symbols) for the NSF [R_{++} (red) and R_{--} (black)] and SF [R_{+-} (green) and R_{-+} (blue)] channels measured from IrMn/CoFe samples at different H_a and for the H_{FG} condition, as indicated. The measurements were done along the first and second field cycles. The arrow in the illustration shows the FM magnetization direction M with respect to the applied field H_a along the y axis. The coordinate system in the plots is left-handed.

$5.0 \mu\text{m}$ after the first half of the second field cycle at H_{C2} . Note that this domain size remains persistently small even during the second half of the first field cycle and also during the first half of the second field cycle (in the trained state as shown in Fig. 7) at H_{C1} .

The interesting aspect that emerges out of the measurements is that coherent rotation of magnetization (uniform reversal) is accompanied by reversal via small-scale domain nucleation and motion (nonuniform reversal). These are identified by an increased SF specular signal and off-specular scattering at the coercive fields. For a typical asymmetric type of reversal, one mechanism dominates the other.

Generally, for nonuniform reversal, the net magnetization is considered to be very close to zero due to a multidomain state with random orientations of magnetization directions. On the other hand, for uniform reversal, the magnetization can turn along the axis perpendicular to the polarization axis in the case of a single domain state. In both cases, the longitudinal

magnetization projection onto the neutron polarization axis (y axis) is proportional to $\langle \cos\phi_A \rangle = 0$, while the transverse component projection (with respect to the polarization axis) onto the x axis is proportional to $\langle \sin^2\phi_A \rangle$. However, in the case of a random distribution of domain magnetization directions, the dispersion is positive ($\langle \cos^2\phi_A \rangle - \langle \cos\phi_A \rangle^2 \neq 0$). For coherent rotation, this dispersion is essentially zero. Thus one can distinguish between a situation of random distribution of nucleated domains and that of a coherent rotation. In the case of smaller domains (smaller than the neutron coherence length along the x axis), one can expect off-specular scattering to show up as well.

In the present case, the net magnetization (ρ_m) at the reversal points is not equivalent to zero but is finite and smaller than that at saturation. This is an indication of the coexistence of uniform and nonuniform reversal mechanisms. Such coexistence is not common in systems with stronger uniaxial anisotropy, e.g., in Co-CoO. Domain structures and their field response are known to be influenced by the uniaxial anisotropy of the system.⁵⁰ Following the value of $\delta\phi_A$ in Table II, one can estimate the degree of training that is evident in the system even as the reversal mechanisms for the two field cycles remain similar.

To illustrate this point, we show in Fig. 8 the spin-asymmetry signal and the SF intensity (linear scale) from the H_{FG} sample at H_{C2} during the first field cycle. The spin asymmetry is given by the ratio of the difference and sum of the NSF signals. Along with the best fitted curves, we also show the patterns simulated for (a) sim_A: $\rho_m = 2.5 \times 10^{-6} \text{ \AA}^{-2}$ (value at saturation) and $\phi_A = -90^\circ$, and (b) sim_B: $\rho_m = 2.5 \times 10^{-6} \text{ \AA}^{-2}$ (value at saturation) and $\phi_A = -20^\circ$. One can see that the simulations are simultaneously not matching the measured NSF and SF data in either case.

2. Sample: H_{FGFC}

The specular reflectivity patterns of the specimen (closed symbols) are plotted together with their least-squares fits (open circle) in Fig. 9 for four different applied fields. A very similar fitting procedure to that shown above is applied. The fits for the first field cycle reveal that the variation of ϕ_A is around -165° at a remanence field, and this turns to $-20^\circ/-110^\circ$ at the respective field values at $H_{C1/C2}$. Similarly, it turns from $-55^\circ/-90^\circ$ when measured along the second field cycle and at respective fields $H_{C1/C2}$, which eventually turns to 0° at saturation. Following the value of $\delta\phi_A$ in Table II, one can see that $\delta\phi_A$ is larger and opposite in sign as compared to that of the H_{FG} sample.

The corresponding intensity maps in Fig. 10 show no off-specular intensities in the untrained or in the trained states. The apparent higher background during the first field cycle intensity is due to the instrumental background conditions during different beamtime schedules and is not related to sample characteristics. This obviously suggests that the magnetization reversal is predominantly via coherent rotation and the domain sizes are larger than the $l_{||}$.

3. Sample: H_{FGIB0}

The specular reflectivity patterns of the specimen (closed symbols) are plotted together with their least-squares fits (open

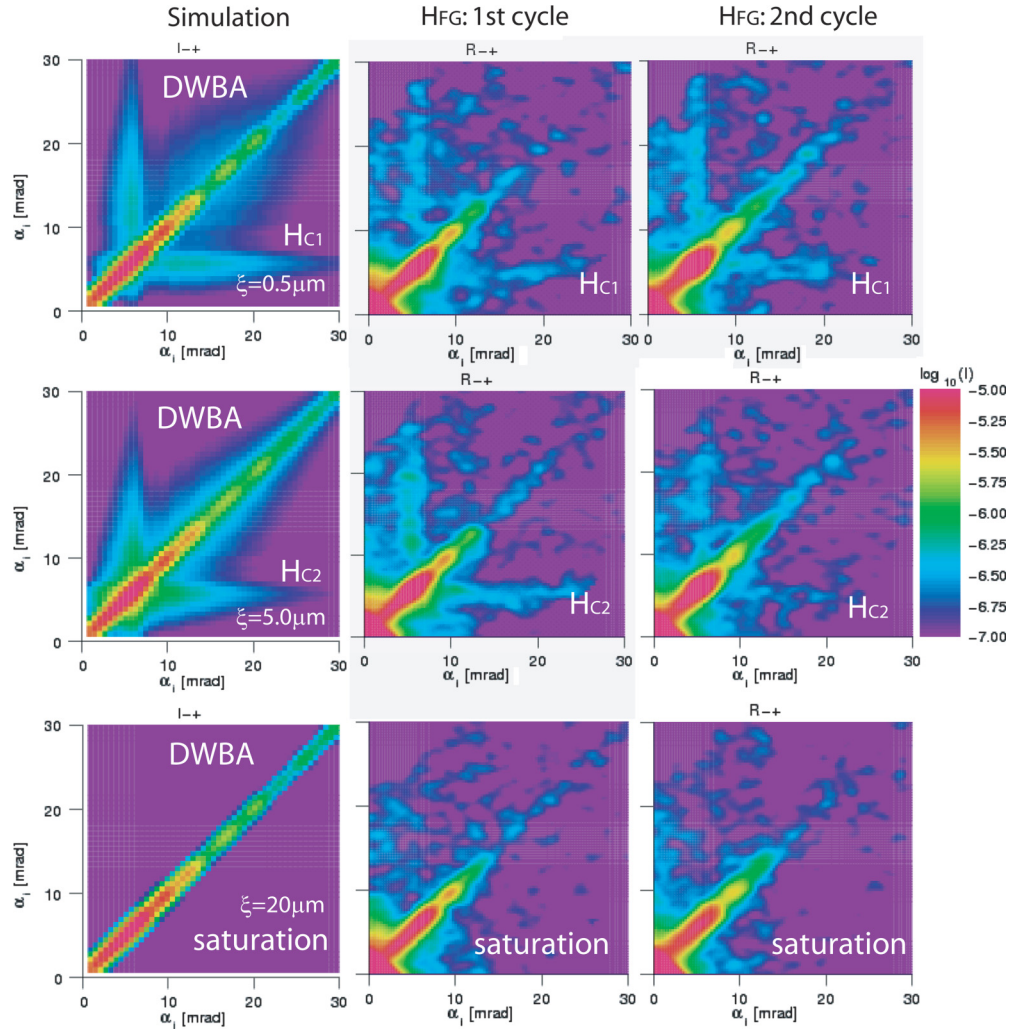


FIG. 7. (Color online) SF intensity maps $[R_{-+}]$ from IrMn/CoFe samples for the H_{FG} condition and measured at H_{C1} along the first half of the first field cycle (untrained), H_{C2} along the second half of the first field cycle, and that at saturation. The measurements for the second field cycle (trained) are also shown alongside.

circle) in Fig. 11 for four different applied fields. The fits for the first field cycle reveal that ϕ_A is $\approx -180^\circ$ at a remanence field and turns to $-130^\circ/-137^\circ$ at the respective field values

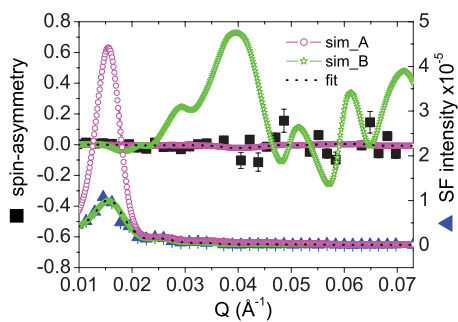


FIG. 8. (Color online) Spin-asymmetry signal (black square) and the SF intensity (blue triangle) from the H_{FG} sample at H_{C2} during the first field cycle. The simulated curves sim_A (magenta circles): $\rho_m = 2.5 \times 10^{-6} \text{ \AA}^{-2}$ and $\phi_A = -90^\circ$, and sim_B (green star): $\rho_m = 2.5 \times 10^{-6} \text{ \AA}^{-2}$ and $\phi_A = -20^\circ$, are plotted along with the best (black dotted) fitted curve.

at $H_{C1/C2}$. Similarly, it turns to $-110^\circ/-145^\circ$ when measured along the second field cycle and at respective fields $H_{C1/C2}$, which eventually turns to 0° at saturation. Following the value of $\delta\phi_A$ in Table II, one can see that it is similar to that of the H_{FG} sample. The corresponding intensity maps (not shown) do not show off-specular intensities confirming the uniform reversal mechanism.

4. Sample: $H_{FGIB180}$

The specular reflectivity patterns of the specimen (closed symbols) are plotted together with their least-square fits (open circle) in Fig. 12 for four different applied fields. The fits for the first field cycle reveal that ϕ_A is $\approx -180^\circ$ at a remanence field and turns to $-30^\circ/-70^\circ$ at the respective field values at $H_{C1/C2}$. Similarly, it turns to $-145^\circ/-70^\circ$ when measured along the second field cycle and at respective fields $H_{C1/C2}$, which eventually turns to 0° at saturation. Following the value of $\delta\phi_A$ in Table II, one can similarly estimate the degree in training which is comparatively larger than for the other specimens but with the same sign as that of the H_{FGFC} specimen. Note that the magnetization rotation

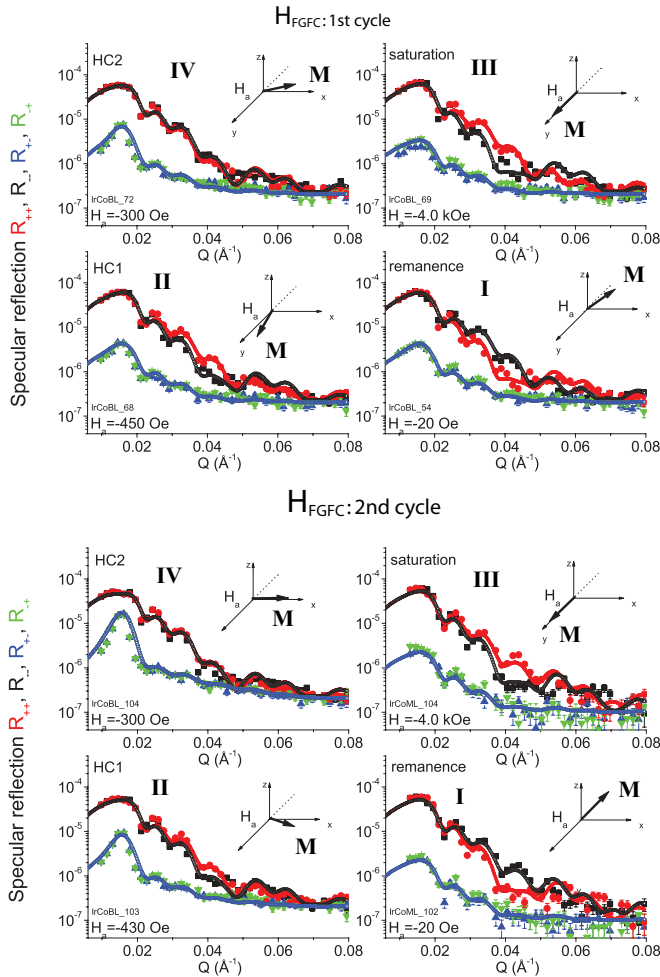


FIG. 9. (Color online) Specular reflectivity patterns (solid symbols) along with their fits (open symbols) for the NSF [R_{++} (red) and R_{--} (black)] and SF [R_{+-} (green) and R_{-+} (blue)] channels measured from IrMn/CoFe samples at different H_a and for the H_{FGFC} condition, as indicated. The measurements were done along the first and second field cycles. The arrow in the illustration shows the FM magnetization direction M with respect to the applied field H_a along the y axis. The coordinate system in the plots is left-handed.

mechanism is the same along the increasing branches of the hysteresis loop (HC_2) for the two field cycles. The absence of off-specular intensities similarly rules out a nonuniform reversal mechanism.

IV. COMPARISON OF RESULTS

The fitted values from the neutron scattering data are presented in Table III. The results show the following:

(i) There are no signatures of asymmetric reversal of magnetization in any of the specimens shown here. Magnetization reversal takes place similarly along both branches of the hysteresis loop irrespective of the biasing conditions.

(ii) Magnetization reversal for the specimen without or with the influence of any external field indicates the coexistence of magnetization reversal via small scale ($\xi \leq l_{\parallel}$) domains and coherent rotation.

(iii) When an external field is applied while cooling the specimens down to RT (H_{FGFC}) or in the presence of irradiating ions (H_{FGIB0} or $H_{FGIB180}$), the magnetization reversal mechanism is predominantly via coherent rotation with no associated signature of small scale domains.

(iv) All specimens at their respective coercive fields exhibit a significant decrease in the magnetic scattering part of their SLD values (ρ_m). Such a decrease indicates a loss of net magnetization due to multiple-domain formation. At the same time, all specimens exhibit a significant increase in their SF signal (which is a measure of the transverse component of magnetization). A reversal via coherent rotation would have rendered no loss of net magnetization at the reversal points. Thus we conclude that all specimens exhibit the formation of 1–10 μm domains and they reverse via coherent rotation. A random noncollinear arrangement of domains is seen as off-specular scattering when they are smaller in size ($\sim 1 \mu\text{m}$) than the neutron coherence length l_{\parallel} .

(v) A partial asymmetric reversal can, however, be seen in the case of H_{FGFC} during the second field cycle. Whereas the reversal along the decreasing branch is via uniform and nonuniform ways, the reversal along the increasing branch is predominantly via the uniform magnetization reversal. This is evident as the net magnetization at HC_2 during the second field cycle is very similar to that in saturation (ρ_m in Table III) while the magnetization direction is perpendicular (ϕ_A in Table II) to the neutron polarization axis.

(vi) The coercive field values H_C (Table I) for the H_{FG} sample are almost twice as large as compared to all the other samples. It is assumed that the FM film is coupled to inhomogeneously distributed random orientations of the easy axes of the AF grains. The reversal mechanism is strongly dependent on the ratio of the coupling between the FM and the AF grains to the intergranular exchange coupling.⁵³ While the irreversible domain state magnetization in the antiferromagnet results in exchange bias, the reversible part of the AF magnetization becomes responsible for the coercivity increase. Thus coercivity enhancement in exchange coupled polycrystalline systems is associated with the number of rotatable AF grains. Our results indicate that there is an increase in the nonrotatable exchange coupled grains upon the extrinsic field applied during the process of cooling and also during ion irradiation as compared to the field grown samples, presumably at the expense of the rotatable ones. This is in accordance with the recently discussed models for thermal drifts of the exchange bias field.^{30,31,33} Note that the change in coercivity, particularly for the H_{FG} specimen (no external biasing condition), from the rest of the specimens is around 100 Oe. Also note that the coercivities for the rest of the specimens (with external biasing conditions) are fairly similar.

(vii) It is also evident that all specimens have undergone training after the first half of the first field cycle. Training is observed in terms of the changing $\delta\phi_A$ (the difference in angular rotation for the first two field cycles) and also the variation of ρ_m with respect to the saturation values and thereby the changes in domain configuration. The degree of training is somewhat similar (considering only $\delta\phi_A$) for all cases except for the $H_{FGIB180}$ sample.

(viii) The sample irradiated with moderate energy (keV) ions, inducing unidirectional anisotropy, does not differ much

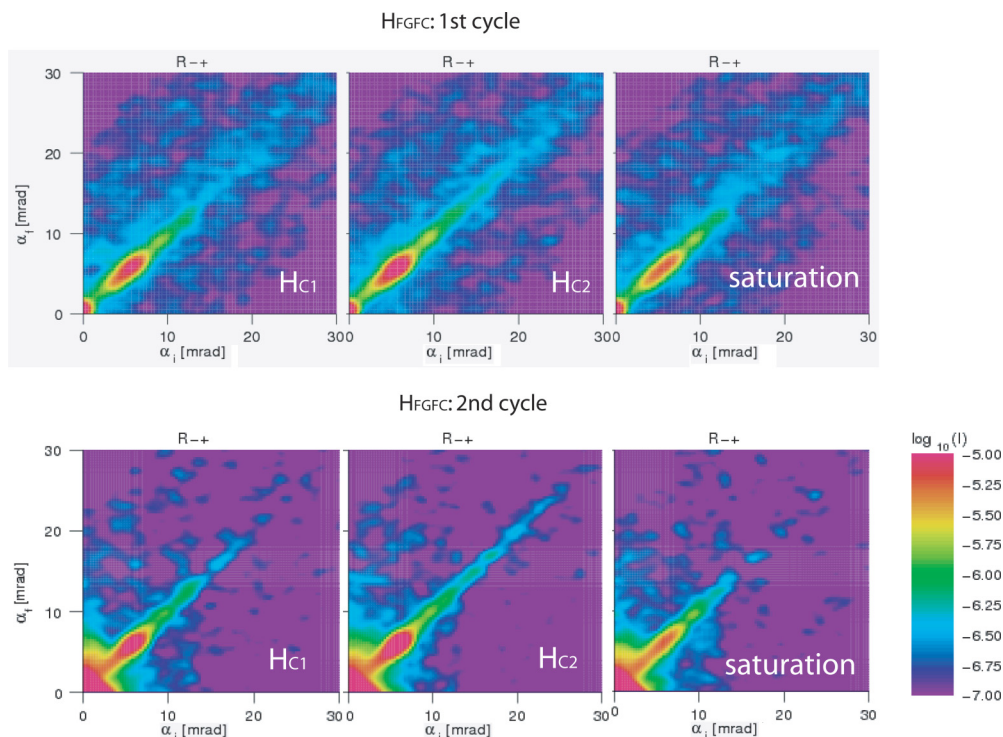


FIG. 10. (Color online) SF intensity maps [R_{-+}] from IrMn/CoFe samples for the H_{FGFC} condition and measured at H_{C1} along the first half of the first field cycle (untrained), H_{C2} along the second half of the first field cycle, and that at saturation. The measurements for the second field cycle (trained) are also shown.

from that induced by field cooling in terms of the reversal mechanism and the associated training. Note that the structural parameters used in the fitting routine for the neutron reflectivity measurements, such as the nuclear SLD ρ_n and the interface roughness, are kept the same for all layers in each of the stack. For an AF thickness of around 10.0 nm (Table II), it can be assumed that the specimens are within the regime where AF domains are believed to have formed or they have a stable uniaxial anisotropy value. The AF anisotropy is presumably not within the range where variations in their blocking temperature (where the bias field H_{EB} disappears) are due to increasing volume of the AF grains. The domain state model predicted the onset of domain formation above a certain thickness of the AF layer.⁵⁴ The changes in the exchange bias values are therefore due to the FM layer thickness and the exchange coupling variations.

(ix) It is interesting to note that the VSM data for the $H_{FGIB180}$ sample do not show any change in the coercive fields. There is no change in the first and also not in the second field cycle. PNR, on the other hand, estimates the largest training along the decreasing branch for the same sample. The training in the $H_{FGIB180}$ sample is about four times larger. This training can be attributed to two biasing conditions induced along opposite directions, one during the growth of the sample and the other during 180° ion irradiation. This has caused a complete reorientation of the AF easy axis with respect to the unidirectional anisotropy axis. Thus it appears that if the deviation of the unidirectional anisotropy is close to the randomly distributed easy axes of the AF grain, then the training is much smaller. However, no training can be seen along the increasing branch.

V. ANISOTROPY ENERGIES

Mauri *et al.*⁵⁵ proposed the domain model of exchange bias way back in 1987. The models of Malozemoff⁵⁶ or the more recent domain state model,⁵⁴ which also introduce domains in the AF layer, are restricted to single crystalline specimens and cannot be extended to polycrystalline ones. Stiles and McMichael proposed a model describing the behavior in polycrystalline specimens. The FM and AF grains are coupled by exchange interactions.⁴ Based upon these, a micromagnetic approach was opted by Saha *et al.*¹³ considering decoupled AF grains in explaining the possibilities for training effects in polycrystalline specimens. According to the granular model of Fulcomer and Charap,⁵⁷ reversal of each grain of the AF is given by the product of its volume and the anisotropy constant. However, none of the model calculations deal with the grain size dependence and the role of anisotropy and their related effect on the bias field and magnetization reversal in general. Model calculations are usually done with strongly anisotropic AF layers or with fourfold (biaxial) in-plane anisotropy.

Mauri *et al.* estimated the AF anisotropy energy via

$$H_{EB} = \frac{t_{AF} K_{AF}}{t_{FM} M_{FM}} \quad (3)$$

assuming that an irreversible switching of the layer will occur for low AF anisotropy systems such as NiO or FeMn and can be considered valid for IrMn as well. Based upon Eq. (2), they had explained the coexistence of exchange field and enhanced coercivity processes in AF-FM layers. This is possible because some portions of the AF regions will follow the FM direction (reversible change), while some

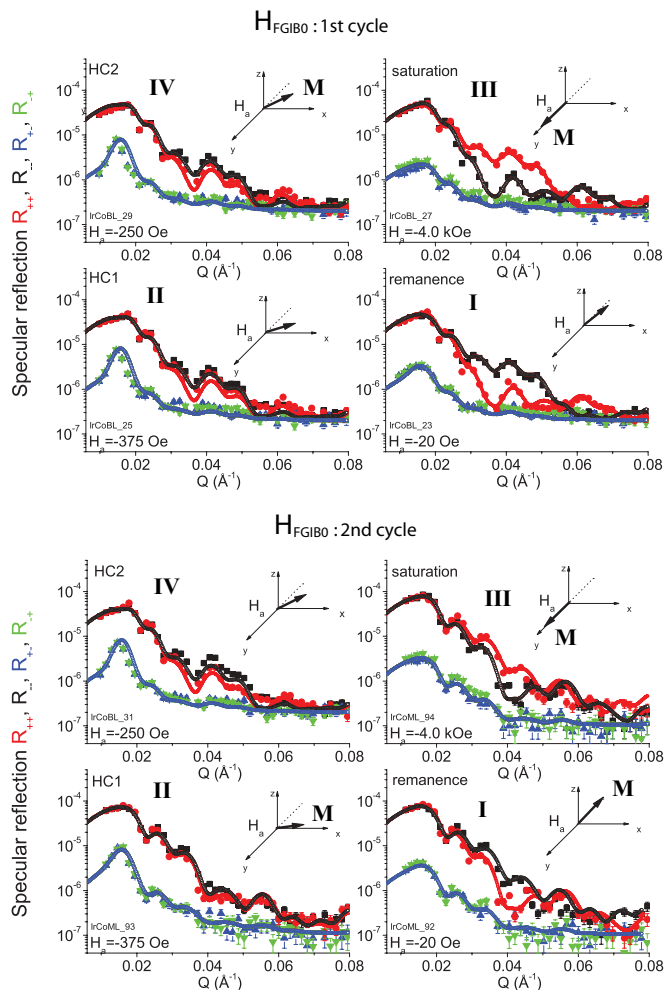


FIG. 11. (Color online) Specular reflectivity patterns (solid symbols) along with their fits (open symbols) for the NSF [R_{++} (red) and R_{--} (black)] and SF [R_{+-} (green) and R_{-+} (blue)] channels measured from IrMn/CoFe samples at different H_a and for the H_{FGIB0} condition, as indicated. The measurements were done along the first and second field cycles. The arrow in the illustration shows the FM magnetization direction M with respect to the applied field H_a along the y axis. The coordinate system in the plots is left-handed.

others will undergo irreversible changes. This coexistence is predicted mainly due to plausible AF grain size distribution. Such grain size distribution is common in polycrystalline samples grown by magnetron sputtering particularly below a critical AF thickness. However, above a critical thickness (~ 10.0 nm), one usually neglects any thermal activation process at room temperature (IrMn Néel temperature $T_N = 690$ K).^{33,58–60} Industrially, AF IrMn is widely used because of the large exchange bias and thermal stability that can be obtained with this material. In our samples, the changes to the magnetic characteristics as a function of time had also attained saturation, and thus the changes for competitive field cycles are not due to thermal fluctuations.

The XRD patterns from our specimens estimate the average grain sizes to be around 5.0–10.0 nm (± 1.0) from the full width at half-maximum (FWHM) IrMn [111] peak using the Scherrer formula.⁶¹ AF anisotropy energies calculated for the four different biasing conditions with a very similar assumption

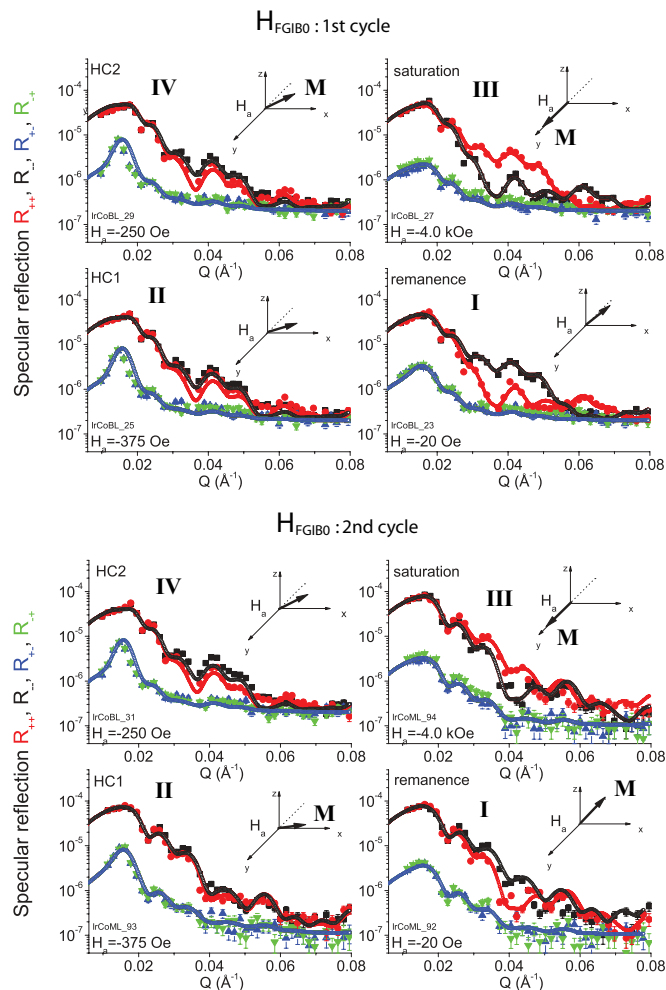


FIG. 12. (Color online) Specular reflectivity patterns (solid symbols) along with their fits (open symbols) for the NSF [R_{++} (red) and R_{--} (black)] and SF [R_{+-} (green) and R_{-+} (blue)] channels measured from IrMn/CoFe samples at different H_a and for the $H_{FGIB180}$ condition, as indicated. The arrow in the illustration shows the FM magnetization direction M with respect to the applied field H_a along the y axis.

render AF anisotropy energies that are an order of magnitude lower ($\sim 10^5$ erg/cm³).

There is no experimental evidence of AF domain formation with the thickness of the AF layer or the stabilization of the AF grain sizes. Nevertheless, we have calculated the energy values using the value of $K_{AF} = 3 \times 10^6$ erg/cm³ (from Ref. 33) for a similar thickness of IrMn. The domain wall energy per unit area is given by $\omega \approx 4\sqrt{A_{AF}K_{AF}}$. The energy for coherent rotation per unit area can be expressed as $\epsilon \sim K_{AF} \times t_{AF}$ (here the thickness is approximated as the grain size, which is of a similar dimension). The domain wall width can be obtained using the expression $L \approx \pi\sqrt{\frac{A_{AF}}{K_{AF}}}$. We have taken IrMn $A_{AF} \sim 9.78 \times 10^{-9}$ erg/cm (for comparison, CoO $A_{AF} \sim 6.96 \times 10^{-7}$ erg/cm) as the exchange stiffness of the AF layer. This follows from the expression for $A_{AF} = \frac{J_{AF}}{a}$, where the IrMn exchange constant $J_{AF} = 0.023$ meV (Ref. 51) [as compared to that of CoO, $J_{AF} = 1.86$ meV (Ref. 52)] and the

TABLE IV. Energy parameters corresponding to two exchange coupled system with different anisotropy values.

Sample	a (Å)	J_{AF} (meV)	A_{AF} (erg/cm)	K_{AF} (erg/cm ³)	L (nm)	ϵ (erg/cm ²)	ω (erg/cm ²)	J_{int} (erg/cm ²)
H_{FGFC}	3.76	0.023 (Ref. 51)	9.78×10^{-9}	5.25×10^6 (Ref. 33)	1.4	4.83	0.9	0.17
CoO/Co	4.27	1.86 (Ref. 52)	6.96×10^{-7}	2.5×10^8 (Ref. 34)	1.7	137	52.9	0.72

IrMn lattice constant $a = 3.76$ Å (as compared to the CoO lattice constant $a = 4.27$ Å).

One can compare the situation for H_{FGFC} with a strongly anisotropic system such as CoO for an AF thickness of 5.0 nm.⁴⁹ The corresponding values are given in Table IV. If the domain wall energy is large, $\omega > J_{int}$, the AF would act as a rigid magnet, preventing the winding up of a domain wall in the AF. This would be the case in which one would expect maximum bias. If the domain wall energy becomes weaker than the interface exchange energy, $\omega < J_{int}$, the bias field would be determined by the formation of a domain wall. In the case of IrMn specimens, the two energies are largely comparable, while for the CoO system they are not. Micromagnetic calculations for a 50.0 nm NiMn AF layer with uniaxial anisotropy, comparable to that of IrMn, also predicted such a reversal mechanism—a comparable contribution of domain nucleation and magnetization rotation resulting in nearly symmetric loop shapes.¹³

The anisotropy energy creates barriers against the free rotation of the magnetization within the magnetic specimen, which lead to energetically preferred directions for the magnetization within individual single-domain grains. Here we observe that the minimum energy path changes from coherent rotation to nucleation followed by domain wall motion until the whole magnetization is reversed. One can see that the energy for coherent rotation is almost similar in magnitude to that of the domain wall energy. This explains the simultaneous observation of a uniform and a nonuniform reversal mechanism in our samples and the symmetric loop shape.

VI. CONCLUSION

We have investigated the training from the first hysteresis loop, or first-loop training. Our samples are chosen such that

they have relatively small uniaxial anisotropy, which can probably be attributed to the buffer layer texture of Cu. Initial nonequilibrium arrangements or metastable states of the AF spins are thereby minimized. We may also neglect any variation of the K_{AF} due to grain size distribution as our AF thickness is above the critical value. Magnetization reversal for the specimen without or with the influence of any external field (either during the cooling process or during ion irradiation) indicates the coexistence of small scale ($\xi \leq l_{||}$) domains and large scale ($\xi \geq l_{||}$) domains. Whereas the smaller domains reverse via nucleation and wall motion, the larger domains reverse via coherent rotation along both branches of the hysteresis loop. Thus a symmetric reversal mechanism is evident for a low anisotropic AF layered system. The training observed here is therefore due to a rearrangement of local anisotropic directions with respect to the applied field direction during growth and/or during the field cooling or ion-irradiation process upon field cycling. Training can be associated with the degree of variation of the mean magnetization direction as well as the variation in the domain configuration. The mechanism of reversal remains similar even during the first-loop training. Training observed by magnetometric methods can often be misleading and obscure. PNR and off-specular scattering measurements together can estimate the degree of training more precisely even when the reversal process is comprised of coherent rotation and domain nucleation and wall movement simultaneously.

ACKNOWLEDGMENTS

This work was supported by the Deutsche Forschungsgemeinschaft via the Transregional Collaborative Research Centers TRR 80.

*Author to whom all correspondence should be addressed: amitesh.paul@frm2.tum.de

¹J. Nogués and I. K. Schuller, *J. Magn. Magn. Mater.* **192**, 203 (1999).

²A. E. Berkowitz and K. Takano, *J. Magn. Magn. Mater.* **200**, 552 (1999).

³W. H. Meiklejohn and C. P. Bean, *Phys. Rev.* **102**, 1413 (1956).

⁴M. D. Stiles and R. D. McMichael, *Phys. Rev. B* **59**, 3722 (1999).

⁵M. Gruyters and D. Schmitz, *Phys. Rev. Lett.* **100**, 077205 (2008).

⁶M. R. Fitzsimmons, P. Yashar, C. Leighton, I. K. Schuller, J. Nogués, C. F. Majkrzak, and J. A. Dura, *Phys. Rev. Lett.* **84**, 3986 (2000).

⁷M. Gierlings, M. J. Prandolini, H. Fritzsche, M. Gruyters, and D. Riegel, *Phys. Rev. B* **65**, 092407 (2002).

⁸A. Paul, E. Kentzinger, U. Rücker, and T. Brückel, *Phys. Rev. B* **74**, 054424 (2006).

⁹A. Paul and S. Mattauch, *Appl. Phys. Lett.* **95**, 092502 (2009); A. Paul, *ibid.* **97**, 032505 (2010).

¹⁰A. Paul and S. Mattauch, *J. Appl. Phys.* **108**, 053918 (2010).

¹¹A. Paul, C. M. Schneider, and J. Stahn, *Phys. Rev. B* **76**, 184424 (2007).

¹²A. Hoffmann, *Phys. Rev. Lett.* **93**, 097203 (2004).

¹³J. Saha and R. H. Victora, *Phys. Rev. B* **76**, 100405(R) (2007); **73**, 104433 (2006).

- ¹⁴B. Beckmann, U. Nowak, and K. D. Usadel, *Phys. Rev. Lett.* **91**, 187201 (2003).
- ¹⁵S. R. Ali, M. R. Ghadimi, M. Fecioru-Morariu, B. Beschoten, and G. Güntherodt, *Phys. Rev. B* **85**, 012404 (2012).
- ¹⁶C. Binek, *Phys. Rev. B* **70**, 014421 (2004).
- ¹⁷D. Engel, A. Kronenberger, M. Jung, H. Schmoranzer, A. Ehresmann, A. Paetzold, and K. Röhl, *J. Magn. Magn. Mater.* **263**, 275 (2003).
- ¹⁸A. Ehresmann, D. Junk, D. Engel, A. Paetzold, and K. Röhl, *J. Phys. D* **38**, 801 (2005).
- ¹⁹M. Gruyters, *Europhys. Lett.* **77**, 57006 (2007).
- ²⁰A. Mougin, T. Mewes, M. Jung, D. Engel, A. Ehresmann, H. Schmoranzer, J. Fassbender, and B. Hillebrands, *Phys. Rev. B* **63**, 060409 (2001).
- ²¹J. Veldeman, H. Jia, and M. Burgelman, *J. Magn. Magn. Mater.* **193**, 128 (1999).
- ²²W. A. A. Macedo, P. L. Gastelois, M. D. Martins, W. Kuch, J. Miguel, and M. Y. Khan, *Phys. Rev. B* **82**, 134423 (2010).
- ²³S. Laureti, S. Y. Suck, H. Haas, E. Prestat, O. Bourgeois, and D. Givord, *Phys. Rev. Lett.* **108**, 077205 (2012).
- ²⁴A. N. Dobrynin and D. Givord, *Phys. Rev. B* **85**, 014413 (2012).
- ²⁵S. R. Ali, M. R. Ghadimi, M. Fecioru-Morariu, B. Beschoten, and G. Güntherodt, *Phys. Rev. B* **85**, 012404 (2012).
- ²⁶X. Martí, B. G. Park, J. Wunderlich, H. Reichlová, Y. Kurosaki, M. Yamada, H. Yamamoto, A. Nishide, J. Hayakawa, H. Takahashi, and T. Jungwirth, *Phys. Rev. Lett.* **108**, 017201 (2012).
- ²⁷Y. G. Wang, A. K. Petford-Long, T. Hughes, H. Laidler, K. O'Grady, and M. T. Kief, *J. Magn. Magn. Mater.* **242**, 1081 (2002).
- ²⁸P. Gogol, J. N. Chapman, M. F. Gillies, and F. W. M. Vanhelfmont, *J. Appl. Phys.* **92**, 1458 (2002).
- ²⁹A. Paetzold and K. Röhl, *J. Appl. Phys.* **91**, 7748 (2002).
- ³⁰A. Ehresmann, C. Schmidt, T. Weis, and D. Engel, *J. Appl. Phys.* **109**, 023910 (2011).
- ³¹C. Schmidt, T. Weis, D. Engel, and A. Ehresmann, *J. Appl. Phys.* **110**, 113911 (2011).
- ³²Y. G. Wang and A. K. Petford-Long, *J. Appl. Phys.* **92**, 6699 (2002).
- ³³N. P. Aley, G. Vallejo-Fernandez, R. Kroeger, B. Lafferty, J. Agnew, Y. Lu, and K. O'Grady, *IEEE Trans. Magn.* **44**, 2820 (2008).
- ³⁴W. L. Roth, *Phys. Rev.* **110**, 1333 (1958).
- ³⁵A. Ehresmann, *Rec. Res. Dev. Appl. Phys.* **7**, 401 (2004).
- ³⁶A. Ehresmann, D. Engel, T. Weis, A. Schindler, D. Junk, J. Schmalhorst, V. Höink, M. D. Sacher, and G. Reiss, *Phys. Status Solidi B* **243**, 29 (2006).
- ³⁷J. Schmalhorst, M. Sacher, V. Höink, G. Reiss, D. Engel, and A. Ehresmann, *Phys. Rev. B* **70**, 184403 (2004).
- ³⁸A. Paul and S. Mattauch, *New J. Phys.* **12**, 103003 (2010).
- ³⁹A. Dunlop and D. Lesueur, *Radiat. Eff. Defects Solids* **126**, 123 (1993).
- ⁴⁰A. Paul and G. S. Lodha, *Phys. Rev. B* **65**, 245416 (2002).
- ⁴¹T. Salditt, T. H. Metzger, and J. Peisl, *Phys. Rev. Lett.* **73**, 2228 (1994).
- ⁴²D. E. Savage, J. Kleiner, N. Schimke, Y. H. Phang, T. Jankowski, J. Jacobs, R. Kariotis, and M. G. Lagally, *J. Appl. Phys.* **69**, 1411 (1991).
- ⁴³L. Daniel, E. Dieter, and E. Arno (unpublished).
- ⁴⁴A. Paul, M. Buchmeier, D. E. Bürgler, U. Rücker, and C. M. Schneider, *Phys. Rev. B* **77**, 184409 (2008).
- ⁴⁵B. P. Toperverg, in *Polarized Neutron Scattering*, Vol. 12 of Matter and Materials (Forschungszentrum Jülich, Germany, 2002), p. 247; H. Zabel *et al.*, in *Handbook of Magnetism and Advanced Magnetic Materials*, edited by H. Kronmüller and S. Parkin (Wiley, New York, 2007), p. 1237.
- ⁴⁶J. F. Ziegler, J. P. Biesack, and U. Littmark, Computer code TRIM, <http://www.srim.org>.
- ⁴⁷L. Nevot and P. Croce, *Rev. Phys. Appl. (France)* **15**, 761 (1980).
- ⁴⁸A. Paul, T. Damm, D. E. Bürgler, S. Stein, H. Kohlstedt, and P. Grünberg, *J. Phys.: Condens. Matter* **15**, 2471 (2003).
- ⁴⁹A. Paul, N. Paul, and S. Mattauch, *New J. Phys.* **13**, 063008 (2011).
- ⁵⁰R. Pulwey, M. Zöfl, G. Bayreuther, and D. Weiss, *J. Appl. Phys.* **91**, 7995 (2002).
- ⁵¹D. Suess, M. Kirschner, T. Schrefl, J. Fidler, R. L. Stamps, and J.-V. Kim, *Phys. Rev. B* **67**, 054419 (2003).
- ⁵²M. D. Reichtin and B. L. Averbach, *Phys. Rev. B* **6**, 4294 (1972).
- ⁵³M. D. Stiles and R. D. McMichael, *Phys. Rev. B* **63**, 064405 (2001).
- ⁵⁴U. Nowak, K. D. Usadel, J. Keller, P. Miltényi, B. Beschoten, and G. Güntherodt, *Phys. Rev. B* **66**, 014430 (2002).
- ⁵⁵D. Mauri, E. Kay, D. Scholl, J. Kent, and J. Kent Howard, *J. Appl. Phys.* **62**, 2929 (1987).
- ⁵⁶A. P. Malozemoff, *Phys. Rev. B* **35**, 3679 (1987).
- ⁵⁷E. Fulcomer and S. H. Charap, *J. Appl. Phys.* **43**, 4190 (1972).
- ⁵⁸K. O'Grady, L. E. Fernandez-Outon, and G. Vallejo-Fernandez, *J. Magn. Magn. Mater.* **322**, 883 (2010).
- ⁵⁹M. Ali, C. H. Marrows, M. Al-Jawad, B. J. Hickey, A. Misra, U. Nowak, and K. D. Usadel, *Phys. Rev. B* **68**, 214420 (2003).
- ⁶⁰V. Baltz, J. Sort, B. Rodmacq, B. Dieny, and S. Landis, *Phys. Rev. B* **72**, 104419 (2005).
- ⁶¹P. Scherrer, *Göttinger Nachrichten Gesell.* **2**, 98 (1918).